Imaging of Fluorescence in Highly Scattering Media

Jenghwa Chang, *Member, IEEE*, Harry L. Graber, *Associate Member, IEEE*, and Randall L. Barbour,* *Member, IEEE*

***Abstract*— Two one-speed radiation transport equations coupled by a dynamic equation for the distribution of fluorophore electronic states are used to model the migration of excitation photons and emitted fluorescence photons. The conditions for producing appreciable levels of fluorophore in the excited state are studied, with the conclusion that minimal saturation occurs under the conditions applicable to tissue imaging. This simplifies the derivation of the frequency response and of the imaging operator for a time-harmonic excitation source. Several factors known to influence the fluorescence response—the concentration, mean lifetime and quantum yield of the fluorophore, and the modulation frequency of the excitatory source—are examined. Optimal sensitivity conditions are obtained by analyzing the fluorescence source strength as a function of the mean lifetime and modulation frequency. The dependence of demodulation of the fluorescent signal on the above factors is also examined. In complementary studies, transport-theory-based operators for imaging fluorophore distributions in a highly scattering medium are derived. Experimental data were collected by irradiating a cylindrical phantom containing one or two fluorophore-filled balloons with continuous wave laser light. The reconstruction results show that qualitatively and quantitatively good images can be obtained, with embedded objects accurately located and the fluorophore concentration correctly determined.**

***Index Terms*— Image reconstruction, luminescent materials/devices, optical imaging, random media, tomography.**

I. Introduction

RADIOLABELED and fluorescent-tagged biomolecules have been successfully used in a range of biomedical research studies for many years. In practical medical imaging, e.g., nuclear medicine and single photon emission tomography (SPECT) and positron emission tomography (PET) imaging, however, only radioisotopes are widely used to provide useful anatomical and physiological information, while use of fluorescent probes in clinical studies has been limited mostly to *in vitro* examination of stained tissue slices. The concentration, the mean lifetime, and the quantum yield of many fluorophores are environmentally sensitive [1], and it should also be possible to exploit these sensitivities in order to derive useful anatomical and physiological information. In particular, we have recognized the advantages of using agents whose environmental sensitivity causes selective activation of fluorescence emission, and we have adopted the term "SAFE imaging" to describe this [2]. The emissivity of a radioisotope is inert to variations in the local chemical and physical environment. In contrast, judicious choice of attached functionalities can produce fluorescent molecules that have: excellent chemical stability and photostability; desired excitation properties in the near infrared region; fluorescent properties that are strongly influenced by, for example, oxygen levels, metal ion concentrations, pH, or lipid composition [3]; and are conjugatable to larger carrier molecules. This combination of attributes produces degrees of freedom not available in radioisotope imaging, in particular significantly greater ability to influence target-to-background ratios. However, the possibility of employing fluorescent probes as substitutes for radioisotopes for thick tissue imaging is complicated by the intense scattering of optical photons. One result of this is that many efficient algorithms developed for X-ray tomography, e.g., any that are based on the Fourier slice theorem [4], [5], are not applicable to the optical imaging problem.

Two formulations commonly used in studies of photon migration in highly scattering media are the radiation transport equation and the diffusion equation. The transport equation [6], [7] is the more physically accurate of the two; its disadvantages include the difficulty or impossibility of obtaining analytic solutions for most problems of practical interest, while the methods available for computing numerical solutions, such as Monte Carlo simulations and discrete ordinates calculations, typically are computation-intensive. The diffusion equation is an asymptotic form of the transport equation [6], [8] which follows from assumptions that are valid at points far from any physical discontinuity and where the differential scattering cross section is at most linearly anisotropic. It has been shown that there are situations where it can be used to accurately and quantitatively describe photon migration in highly scattering media [9]–[11]. Wu *et al.* [12] and Patterson *et al.* [13] also have successfully applied it to the problem of describing patterns of fluorescence in highly scattering media. In some cases, e.g., homogeneous infinite, half-space, or slab media, the diffusion equation has analytic solutions in the frequency domain. A major drawback to the diffusion approach is that its solutions are physically inaccurate in the vicinity of a boundary or where the medium's properties vary rapidly in space. In addition, Larsen [14] has compared calculations of the spread of a penetrating pencil beam obtained from both the diffusion equation and the transport equation, and concluded that the relative magnitudes of distortions in the diffusion solution generally grow with the size of the system and can be as

Manuscript received February 15, 1996; revised April 1, 1997. This work was supported in part by the National Institutes of Health, under Grant RO1-CA59955; the New York State Science and Technology Foundation; and the Office of Naval Research(ONR) under Grant N000149510063. *Asterisk indicates corresponding author.*

J. Chang is with the Department of Pathology, SUNY Health Science Center at Brooklyn, Brooklyn NY 11203 USA.

H. L. Graber is with the Department of Physiology and Biophysics, SUNY Health Science Center at Brooklyn, Brooklyn NY 11203 USA.

*R. L. Barbour is with the Department of Pathology and the Department of Physiology and Biophysics, SUNY Health Science Center at Brooklyn, Box 25, 450 Clarkson Avenue, Brooklyn, New York 11203 USA (e-mail: rbarbour@netmail.hscbklyn.edu).

Publisher Item Identifier S 0018-9294(97)06108-9.

high as 90%. Because of these considerations, our group has focused primarily on the transport equation [15]–[17], as in the present study, but has also adopted the diffusion approach when it is appropriate [18]–[20].

One issue explored in this paper, which is an expanded version of two recent conference reports [21], [22], is to analytically explore the effects of saturation and demodulation on a source of fluorescence photons in order to determine conditions for optimal sensitivity to changes in its properties. Saturation is a consequence of the finite lifetime of a fluorophore's excited state [23] and is problematic because it causes coupling among the modulation frequency and its overtones, thus, affecting interpretation of the detected signals. The sensitivity, by which we mean the rates of change in observable quantities such as the amplitude and phase of the emitted light with respect to changes in the fluorophore's physical properties, directly determines the target detectability and signal quality, and is generally a function of lifetime, modulation frequency, and the properties of the background medium [18], [19]. While some extensive numerical or experimental studies addressing the issue of sensitivity for specific types of target and background media have been performed [24], [25], we believe that a theoretical analysis of the emission source itself should provide useful information. In both studies just cited, for example, two different fluorophores with distinct mean lifetimes and fixed quantum yields were used, with one located in the target region and the other in the background. Here, we explore the sensitivity of a truly *environment-sensitive* fluorophore. By this we mean, a fluorophore whose *intrinsic* lifetime is fixed and whose mean lifetime and quantum yield may change as a function of environmental parameters (e.g., tissue oxygen pressure, pH). We have elected to study the properties of the light emitted by an environment-sensitive fluorescent compound directly illuminated by an excitation source, in the absence of any background medium that modifies, through its own absorption and scattering, the excitation light reaching the fluorophore or the fluorescence that ultimately is seen by a detector. We do not mean to minimize the importance of the background medium's effects, but choose to omit it in this study because its properties typically are unknown and its effects are case-dependent.

Our secondary purpose is to present images reconstructed from experimental data obtained from a highly scattering medium containing fluorescent inclusions and illuminated by a dc source. Optical imaging of tissues using tomographic illumination and detection schemes has attracted significant interest in recent years [26], [27]. In most cases, perturbation methods are used for analysis of time-resolved, time-harmonic, or continuous-wave (CW) measurements. This approach analyzes the difference between measurements obtained at the boundary of reference and test media and uses this information to reconstruct two-dimensional (2-D) or three-dimensional images of the differences between them. The difference signal is usually small relative to the two quantities being compared, and it is sensitive to noise. Use of fluorescent light for optical imaging of tissues, on the other hand, has several important advantages. First, is the fact that fluorescence measurements are intrinsically much more sensitive than absorption/scattering measurements. This is because, in the absence of the fluorophore, which itself is the perturbing agent, the reference intensity is zero. Other advantages include the fact that the physical properties of a fluorophore can be sensitive to its immediate chemical environment. Thus, a fluorescence tomography method has properties similar to magnetic resonance imaging (MRI) but at a sensitivity level orders of magnitude greater. The reason for this is that all fluorophore molecules can contribute to the measured fluorescence, while the net MRI signal comes from only the small excess of atoms that are in the low-energy magnetization state at commonly employed external magnetic field strengths [28]. In addition, by linking the fluorophore to a targeting biomolecule (e.g., a monoclonal antibody) the fluorescence tomography method becomes similar to radioscintigraphic imaging methods but without the need for exposure to ionizing radiation. Images reconstructed from numerical data have been published by O'Leary *et al.* [29], Paithankar *et al.* [30], and our group [17]. The new experiments described here were performed under CW illumination, and reconstructed images of the fluorescence concentration are reported in this study.

We use two coupled one-speed transport equations in our theoretical study of fluorescence. The equation governing the fractional excited state fluorophore concentration was also studied, and upper limits to the excitation intensity for which saturation effects may be neglected were determined in order to simplify the problem. The sensitivity of the fluorescence emission to changes in the mean lifetime and modulation frequency, and the effect of the demodulation caused by the fluorophore's lifetime distribution were studied. Further, we derived an imaging operator based on transport theory. The final form of this operator is a system of linear equations which can be easily solved by iterative methods. Monte Carlo simulations were performed to calculate this operator for a specific test medium. Experimental data were collected using a CT-type scanning laser system. Image reconstructions were performed using projection onto convex sets (POCS) [31], conjugate gradient descent (CGD) [32], and simultaneous algebraic reconstruction technique (SART) [4] methods.

II. Theory

We present here a theoretical treatment of the excitation and fluorescence intensities that does not consider fluorescence polarization or other anisotropic phenomena. Modulated light propagation in a material can be described by the Fourier transformed time-dependent radiative transfer equation (RTE) [6]–[8], [33]

$$\frac{j\omega\tilde{\phi}}{c} + \mathbf{\Omega}\cdot\nabla\tilde{\phi} + \mu_T\tilde{\phi} = \tilde{S} + \int_0^\infty \int_{4\pi} \mu_s(\mathbf{r}, \mathbf{\Omega}'\cdot\mathbf{\Omega}, E' \to E)\tilde{\phi}'\, d\Omega'\, dE' \quad (1)$$

where "$\sim$" indicates the Fourier transform (FT), ω is the modulation radial frequency [rad s^{-1}], c is the speed of light [cm s^{-1}], E is the photon energy [eV], $d\Omega'$ is the differential solid angle [sr], $\phi = \phi(\mathbf{r}, \mathbf{\Omega}, E, \omega)$ is the angular intensity (or radiance) [cm^{-2} sr^{-1}], $\phi' = \phi(\mathbf{r}', \mathbf{\Omega}', E', \omega)$, $S =$

$S(\mathbf{r}, \mathbf{\Omega}, E, \omega)$ is the angular source strength [cm^{-3} sr^{-1}], $\mu_s(\mathbf{r}, \mathbf{\Omega}' \cdot \mathbf{\Omega}, E' \rightarrow E)$ is the macroscopic differential scattering cross section [cm^{-1} sr^{-1} eV^{-1}], $\mu_T = \mu_T(\mathbf{r}, E)$ is the macroscopic total cross section [cm^{-1}], and $j = \sqrt{-1}$. We can assume without loss of generality that the excitation and emitted light are monoenergetic with energies E_1 and E_2, respectively. (For detailed discussion, see [17].) Then (1) reduces to two coupled equations. For the excitation angular intensity

$$\frac{-j\omega\tilde{\phi}_1}{c} + \mathbf{\Omega} \cdot \nabla \tilde{\phi}_1 + (\mu_{T,1} + \mu_{T,1\rightarrow 2})\tilde{\phi}_1 = \tilde{S}_1 + \int_{4\pi} \mu_{s,1}(\mathbf{\Omega}' \cdot \mathbf{\Omega})\tilde{\phi}_1' \, d\Omega' \quad (2)$$

where $\mu_{T,1}$ is the total cross section of the reference medium for E_1 and $\mu_{T,1\rightarrow 2}$ is the change in total cross section after the fluorophore is added. That is, $\mu_{T,1\rightarrow 2} = N_g \sigma_{T,1\rightarrow 2}$, where $\sigma_{T,1\rightarrow 2}$ is the microscopic total cross section [cm^2] of the fluorophore and $\tilde{N}_g$ is the FT of the time-dependent concentration of the fluorophore in the ground state. This, in turn, is governed by

$$-j\omega\tilde{N}_g = -\sigma_{T,1\rightarrow 2}\tilde{\bar{\phi}}_1 \otimes \tilde{N}_g + \frac{1}{\tau}\tilde{N}_e \quad (3)$$

where "$\otimes$" denotes a convolution in frequency, $\tilde{N}_e = \tilde{N}_0 - \tilde{N}_g$ is the FT of the time-dependent concentration of the excited fluorophore, $\tilde{N}_0$ is the FT of the total fluorophore concentration (ground and excited electronic states), $\tilde{\bar{\phi}}_1 = \tilde{\bar{\phi}}_1(\mathbf{r}, \omega) = \int_{4\pi} \tilde{\phi}_1 \, d\Omega$ is the FT of the time-dependent intensity (or fluence rate) [cm^{-2}] of the excitation light, and τ is the mean lifetime of the fluorescent probe's excited state. The RTE for the fluorescence angular intensity is

$$\frac{-j\omega\tilde{\phi}_2}{c} + \mathbf{\Omega} \cdot \nabla \tilde{\phi}_2 + \mu_{T,2}\tilde{\phi}_2 = \tilde{S}_2 + \int_{4\pi} \mu_{s,2}(\mathbf{\Omega}' \cdot \mathbf{\Omega})\tilde{\phi}_2' \, d\Omega' \quad (4)$$

where $\tilde{S}_2 = \gamma\tilde{N}_e/4\pi\tau$, $\gamma = \tau/\tau_0$ is the quantum efficiency [dimensionless] and τ_0 is the intrinsic mean lifetime [s] of the fluorescent probe's excited state.

In an ideal case, where only one fluorophore species is present in a homogeneous environment, (3) implies that the temporal impulse response of N_e is a simple exponential decay. However, multiexponential decay can be observed for a mixture of fluorophores with different mean lifetimes, or for a single fluorophore species in a heterogeneous environment. In this study, we consider the cases of a single fluorophore in a heterogeneous environment and of a mixture of two or more fluorophore species whose emissions can be excited or detected *separately*.

III. Saturation Condition, Sensitivity, and Demodulation for a Modulated Waveform

A. Saturation

Inspection of (3) shows that in the frequency domain the ground state fluorophore concentration is a function of the convolution of the concentration itself and the excitation field intensity. Because of this, a time-harmonic excitation will produce an *an*harmonic periodic signal containing the fundamental frequency and all its overtones; this occurs when the population of the excited state becomes appreciable, i.e., when the fluorophore is partially saturated. This situation is problematic because subsequent analysis to infer properties of an unknown medium would require consideration of all these frequencies.

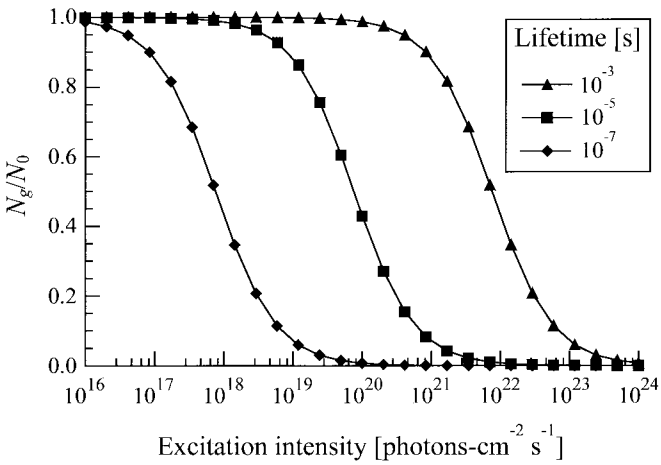

Fig. 1. Fluorophore saturation as a function of excitation intensity for different mean lifetimes [s] and assuming a fluorophore molar extinction coefficient of 3.47×10^5 cm^{-1} M^{-1}. Unless τ is very large, there is no appreciable saturation at excitation intensity levels normally used in biological applications ($\leq 10^{20}$ photons $\cdot$ cm^{-2} s^{-1}, assuming a beam of 0.1 cm in diameter and at most 0.1 W illumination at 1.0 μm wavelength).

If the extent of fluorophore saturation is negligible, then $\tilde{N}_g \approx \tilde{N}_0$. For CW excitation $\tilde{\bar{\phi}}_1 = 2\pi\phi_1^0\delta(\omega)$, where ϕ_1^0 is the excitation intensity. In this case, (3) becomes $0 = -\sigma_{T,1\rightarrow 2}\phi_1^0\tilde{N}_g + (\tilde{N}_0 - \tilde{N}_g)/\tau$, or $\tilde{N}_g = \tilde{N}_0/(1+\tau\sigma_{T,1\rightarrow 2}\phi_1^0)$, which reduces to $\tilde{N}_g \approx \tilde{N}_0$ when $\tau\sigma_{T,1\rightarrow 2}\phi_1^0 \ll 1$. Fig. 1 shows saturation versus excitation intensity curves for different mean lifetimes. If we choose arbitrarily a level of 1% fluorophore saturation as our negligibility threshold, then the maximum allowable excitation is $\phi_1^0 = 1/99\tau\sigma_{T,1\rightarrow 2}$. For a fluorescent dye with a molar extinction coefficient ε of $\sim 10^4$ cm^{-1}M^{-1} [ε and $\sigma_{T,1\rightarrow 2}$ are related by $\varepsilon = A_0\sigma_{T,1\rightarrow 2}/(10^3 \ln 10)$, where A_0 is Avogadro's number, 6.022×10^{23}mol^{-1}] and a mean lifetime $<10^{-7}$ s, the acceptable excitation intensity is $\sim 10^{21}$ photons-cm^{-2} s^{-1}, which is much larger than the excitation intensity levels normally used in biological applications ($\leq 10^{20}$ photons-cm^{-2} s^{-1}, assuming a beam of 0.1-cm diameter and at most 0.1 W illumination power at a wavelength of 1.0 μm).

B. Optimal Modulation Frequency and Mean Lifetime for Optimal Sensitivity

There are two necessary conditions for successful detection of mean lifetime perturbations by means of a fluorescence measurement. The first is that the perturbation must produce an appreciable change in some property of the emissive source (e.g., dc intensity, ac amplitude, or ac phase). The

second is that this change must have an appreciable impact on one or more detector readings. The emissive source is a function of the concentration, molar extinction coefficient, mean lifetime and quantum yield of the fluorophore, and of the excitation intensity. The background medium is not itself affected by the fluorophore, but behaves like a filter that modifies the excitation and emission fields through scattering and absorption. The expression we used in the computation of expected detector response for a time-harmonic source, given the physical properties of the background medium, fluorophore concentration, and lifetime and quantum yield is given in a subsequent section.

The source term for fluorescence is

$$\begin{aligned}\tilde{S}_2 &= \frac{\gamma \tilde{N}_e}{4\pi\tau} \\ &= \frac{\gamma \sigma_{T,\,1\to 2} N_0 \tilde{\bar{\phi}}_1}{4\pi(1+j\omega\tau)} \\ &= \frac{\tau \sigma_{T,\,1\to 2} N_0 \tilde{\bar{\phi}}_1}{4\pi\tau_0\sqrt{1+\omega^2\tau^2}}\, e^{-j\,\tan^{-1}\omega\tau} \\ &\equiv A e^{-j\varphi}. \end{aligned} \tag{5}$$

Let τ_0 be fixed while τ varies because of spatial and/or temporal variations in the nonradiative de-excitation rate of the excited fluorophore. Fig. 2 shows the dependence on τ of the amplitude, A, and phase, φ, of $\tilde{S}_2$. Inspection of Fig. 2 reveals that the source term for fluorescent emission is more sensitive to changes in τ for shorter-lived fluorophores. This observation can be verified by comparing the limiting forms of (5) for very large or very small $\omega\tau$. That is, when $\omega\tau \ll 1$, $S_2 \approx [\tau\sigma_{T,\,1\to 2} N_0 \tilde{\bar{\phi}}_1/(4\pi\tau_0)]e^{-j\omega\tau}$, which is a function of τ, while when $\omega\tau \gg 1$, $S_2 \approx [\gamma\sigma_{T,\,1\to 2} N_0 \tilde{\bar{\phi}}_1/(4\pi\omega\tau)]e^{-j\pi/2} = -j\sigma_{T,\,1\to 2} N_0 \tilde{\bar{\phi}}_1/(4\pi\omega\tau_0)$, which is independent of τ.

The sensitivity of the emissive source to the mean lifetime can be defined in terms of the derivatives of the fluorescence source's amplitude and phase with respect to τ, that is, as $B(\partial A/\partial\tau) = 1/(1+\omega^2\tau^2)^{3/2}$, where $B \equiv 4\pi\tau_0/(\sigma_{T,\,1\to 2} N_0 \tilde{\bar{\phi}}_1)$, and $-\partial\varphi/\partial\tau = \omega/(1+\omega^2\tau^2)$. These are our preferred definitions of sensitivity when we wish to determine the absolute change in τ caused by a change in the environment, regardless of the reference mean lifetime. On the other hand, when changes in τ roughly proportional to the reference mean lifetime are expected, $\tau B(\partial A/\partial\tau)$ and $-\tau(\partial\varphi/\partial\tau)$ may be better indicators of sensitivity. To explore the optimal combinations of modulation frequency and mean lifetime under each definition, both sets of sensitivity measures were derived and are plotted against modulation frequency f [s^{-1}], where $f = \omega/2\pi$, in Fig. 3. The curves shown in Fig. 3(a) and (b) are A (normalized by setting the greatest value equal to 1.0) versus f and φ versus f for three different mean lifetimes, assuming a τ_0 of 10^{-8} s. Fig. 3(c) and (d) shows the corresponding curves for $B(\partial A/\partial\tau)$ and $-\partial\varphi/\partial\tau$, while Fig. 3(e) and (f) shows $\tau B(\partial A/\partial\tau)$ and $-\tau(\partial\varphi/\partial\tau)$.

Inspection of Fig. 3(a) and (b) indicates that the maximum amplitude and minimum phase lag occur at dc (i.e., $f = 0$), and the amplitude decreases while the phase lag increases with increasing f for all three mean lifetimes. The optimal sensitivity, when defined as the fs at which $B(\partial A/\partial\tau)$ and $-\partial\varphi/\partial\tau$ are maximal, occurs at dc for the amplitude, and is a function of τ for the phase, as shown in Fig. 3(c) and (d). When selecting the f to work with in practice, it is necessary to choose a compromise value between dc and the optimal f for the phase. The latter we define as the positive, finite modulation frequency for which $\partial^2\varphi/\partial\omega\partial\tau = 0$. This is $\omega = 1/\tau$, or $f \approx 0.159/\tau$; the corresponding maximum value of $-\partial\varphi/\partial\tau$ is $1/(2\tau)$. The complementary question is what value of τ gives the greatest sensitivity at a fixed f. It is apparent in Fig. 3(c) and (d) (and can be shown analytically) that for any f, amplitude and phase sensitivity both decrease monotonically with increasing τ.

The choice of optimal mean lifetime and modulation frequency is more complicated under the definition of sensitivity as $\tau B(\partial A/\partial\tau)$ and $-\tau(\partial\varphi/\partial\tau)$, as inspection of Fig. 3(e) and (f) reveals. It is straightforward to show that at a fixed τ the optimal fs are the same under these definitions of sensitivity as under the previous ones: $f = 0$ for amplitude and $f \approx 0.159/\tau$

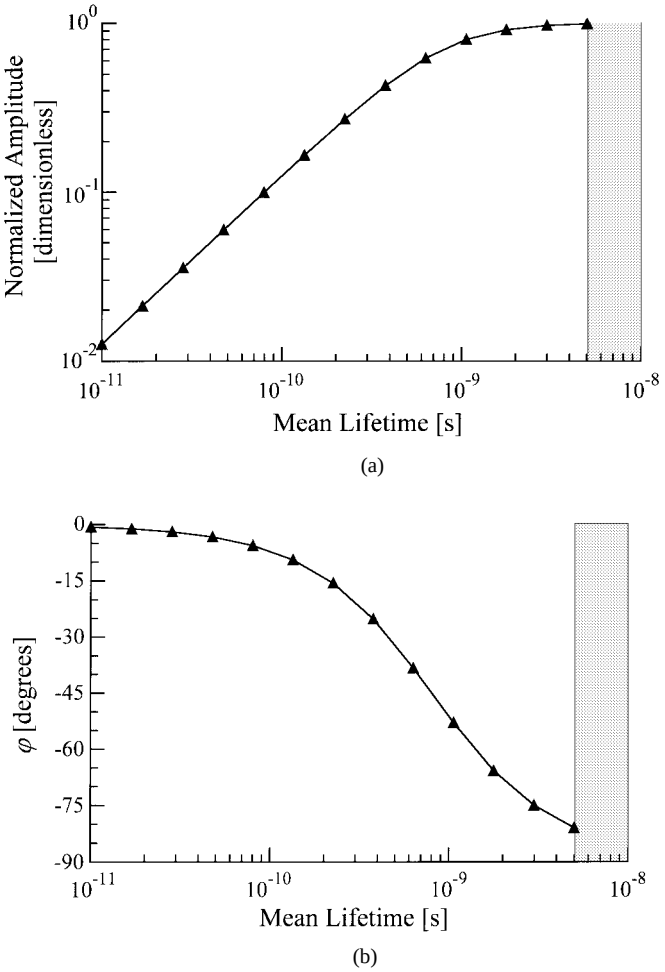

Fig. 2. Amplitude (normalized, logarithmic scale) and phase, φ, of the effective emission source, S_2, as a function of mean lifetime [s] (logarithmic scale) at modulation frequency $f = 200$ MHz. Assumes that $\tau_0 = 5 \times 10^{-9}$ s, $\bar{\phi} = 10^{18}$ cm^{-2}, $\varepsilon = 2 \times 10^{5}$ cm^{-1}M^{-1}, and $N_0 = 6 \times 10^{13}$ cm^{-3}. Therefore, the quantum yield falls in direct proportion to the mean lifetime. The shaded regions, in which $\tau > \tau_0$, are physically inaccessible.

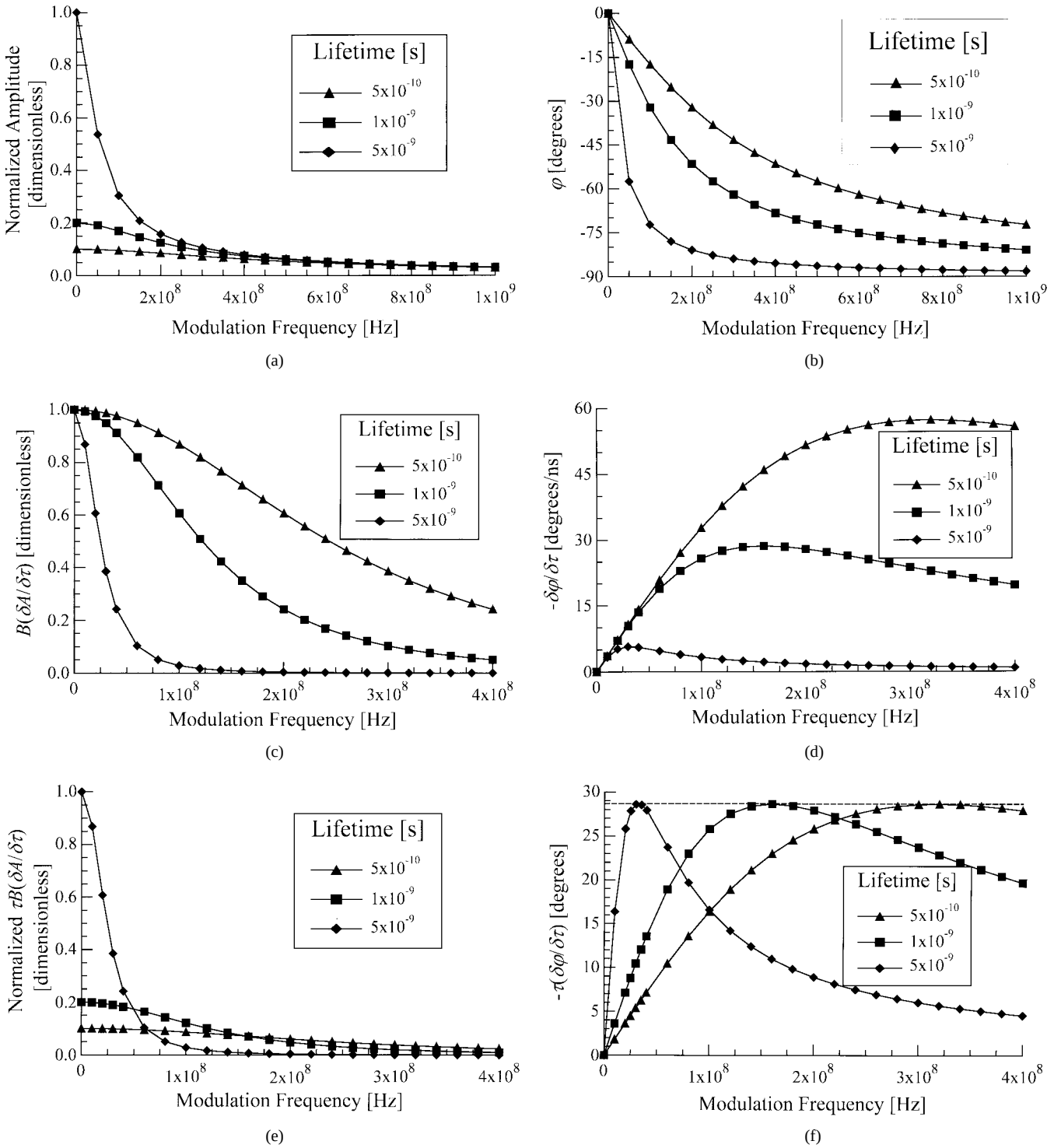

Fig. 3. (a) Amplitude (normalized) and (b) phase, φ, of the emission source intensity as a function of mean lifetime [s] and modulation frequency [Hz]. Assumes that $\tau_0 = 5 \times 10^{-9}$ s, $\bar{\phi} = 10^{18}$ cm^{-2}, $\varepsilon = 2 \times 10^5$ cm^{-1}M^{-1}, and $N_0 = 6 \times 10^{13}$ cm^{-3}, (c) $B(\partial A/\partial\tau)$ versus f, where $B = 4\pi\tau_0/(\sigma_{T,\,1\to 2}N_0\bar{\phi}_1)$; (d) $-\partial\varphi/\partial\tau$ versus f; (e) $\tau B(\partial A/\partial\tau)$ versus f; (f) $-\tau(\partial\varphi/\partial\tau)$ versus f, all curves have the same absolute maximum value.

for phase. Under these sensitivity definitions, however, all fluorophores have the same maximum phase sensitivity, $\frac{1}{2}$ rad $\approx 28.65°$. We also see that long-lived fluorophores have greater amplitude and phase sensitivities than do short-lived ones at low modulation frequencies, but that this trend reverses as f increases. It is optimal to pair long(short)-lived fluorophores with low(high) modulation frequencies; it can be shown analytically that for a fixed f the amplitude sensitivity is greatest for a fluorophore with $\tau = 1/(\sqrt{2}\omega) \approx 0.113/f$, and the phase sensitivity is greatest for one with $\tau = 1/\omega \approx 0.159/f$.

C. Demodulation and Detectability

The factor $\sqrt{1+\omega^2\tau^2}$ which appears in the denominator of the expression for the emissive source amplitude A in (5)

gives the mathematical form of the demodulation effect that is seen as the modulation frequency increases. In addition to the role it plays in determining the sensitivity of the emissive source amplitude to changes in τ treated above, demodulation also places an practical upper limit on the usable modulation frequency. This is because in practice the detected signal consists of a sum of ac and dc components; it is the strength of the dc signal which determines the sensitivity setting of the detecting instrument (e.g., the V/Div setting on an oscilloscope), and thereby the minimum detectable A. If we assume that the excitation field modulation is 100%, then the emissive source modulation is

$$M \equiv \left|\frac{S_2(\omega)}{S_2(0)}\right| = \frac{1}{\sqrt{1+\tau^2\omega^2}}. \tag{6}$$

Thus, to achieve a high modulation, both the mean lifetime and the modulation frequency should be as low as possible. A rule of thumb can be derived for a given dynamic range of mean lifetimes. If we choose 10% as an acceptable threshold for modulation, then $1/\sqrt{1+(2\pi f\tau)^2} \geq 0.1$, which leads to $f \leq \sqrt{99}/(2\pi\tau) \approx 1.584/\tau$.

IV. The Inverse Problem

A. Inversion Formula for DC Source

The goal of the inverse problem is to solve (5) for $\mu_{T,\,1\to 2}$, γ, and τ under different source and detection conditions. In this section an inversion formula for reconstruction of the quantity $\gamma\mu_{T,\,1\to 2}$ from CW fluorescence data is introduced, and reconstructions based on experimental data are presented. The detailed derivation of inversion formulas for the negligible-saturation case [17] is summarized in the following. Let $\tilde{R}$ be the reading of a given detector for the light emitted by the fluorescent source, $\tilde{G}_2(\mathbf{r}, \mathbf{\Omega}; \mathbf{r}', \mathbf{\Omega}'; \omega)$ the frequency-domain Green's function for the fluorescence detected at $\mathbf{r}$ in direction $\mathbf{\Omega}$ when the source is located at $\mathbf{r}'$ in direction $\mathbf{\Omega}'$, and $\tilde{r}_2 = \tilde{r}_2(\mathbf{r}, \mathbf{\Omega}, E, \omega)$ the detector sensitivity function at the wavelength of the emitted light. Applying a well-known reciprocity theorem [34], $\tilde{G}_2(\mathbf{r}, \mathbf{\Omega}; \mathbf{r}', \mathbf{\Omega}'; \omega) = \tilde{G}_2(\mathbf{r}', -\mathbf{\Omega}'; \mathbf{r}, -\mathbf{\Omega}; \omega)$, and letting $\omega = 0$, we obtain the detector readings for a CW source as

$$\begin{aligned}\tilde{R} &= \int_V \frac{\tilde{\tilde{\phi}}_1 \tilde{\tilde{\phi}}_2^{+}}{4\pi} \frac{\gamma\sigma_{T,\,1\to 2} N_0 e^{-j\,\tan^{-1}\omega t}}{\sqrt{1+\omega^2\tau^2}}\, d^3r \\ &\xrightarrow{\omega=0} \int_V \frac{\tilde{\tilde{\phi}}_1 \tilde{\tilde{\phi}}_2^{+}}{4\pi} (\gamma N_0 \sigma_{T,\,1\to 2})\, d^3r \\ &= \int_V w(\gamma N_0 \sigma_{T,\,1\to 2})\, d^3r \end{aligned} \tag{7}$$

where $\tilde{\tilde{\phi}}_2^{+} = \int_{4\pi}\int_{V'}\int_{4\pi} \tilde{r}_2' \tilde{G}_2(\mathbf{r}, -\mathbf{\Omega}; \mathbf{r}', -\mathbf{\Omega}'; 0)\, d\mathbf{\Omega}'\, d^3r'\, d\omega$ is the adjoint intensity and $w \equiv w_{\mathrm{dc}} = \tilde{\tilde{\phi}}_1 \tilde{\tilde{\phi}}_2^{+}/4\pi$ is the weight function. If $\sigma_{T,\,1\to 2}$ is known and $\tilde{\tilde{\phi}}_1$ and $\tilde{\tilde{\phi}}_2^{+}$ can be precalculated under the assumption that fluorophore is not present, then the unknown quantity γN_0 can be computed by solving a linear system obtained by discretizing (7). Here, only the product of quantum efficiency and fluorophore concentration is found, and they can not be directly separated. More complete derivations of the inverse formulas for reconstruction of the mean lifetime are available in [17] for both the negligible-saturation and appreciable-saturation cases.

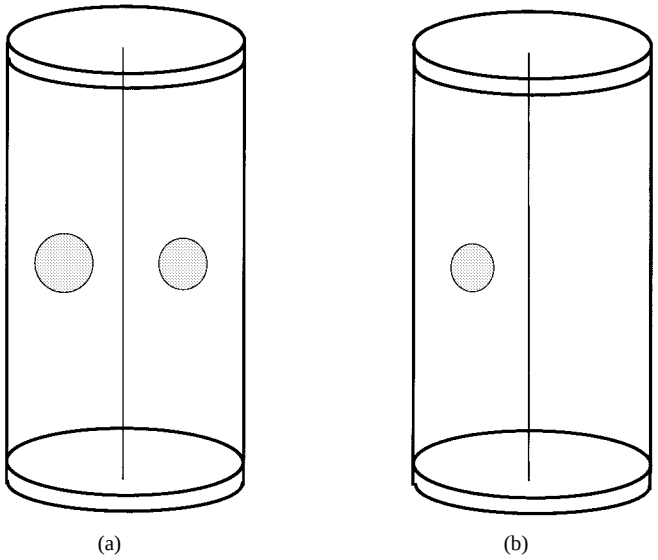

Fig. 4. (a) Tissue phantom for the first experiment, where two balloons were suspended in the cylinder and (b) phantom for the second experiment, where only one balloon was used.

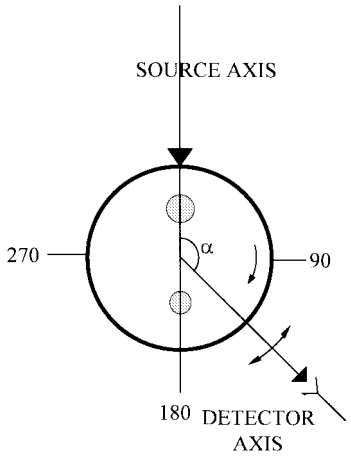

Fig. 5. Source and detector configurations.

B. Experimental Setup

The experimental tissue phantoms are sketched in Fig. 4, and the source and detector configurations in Fig. 5. In these initial studies we have sought to evaluate the imaging scheme using a time-independent source. Two experiments were performed, one with two balloons containing a fluorescent dye and no dye in the background, the other with a single dye-filled balloon and the same dye at a lower concentration added to the background. In the first experiment, balloons containing different volumes (0.8 and 1.2 mL) of Rhodamine 6G dye (peak emission at ~590 nm) at a concentration of

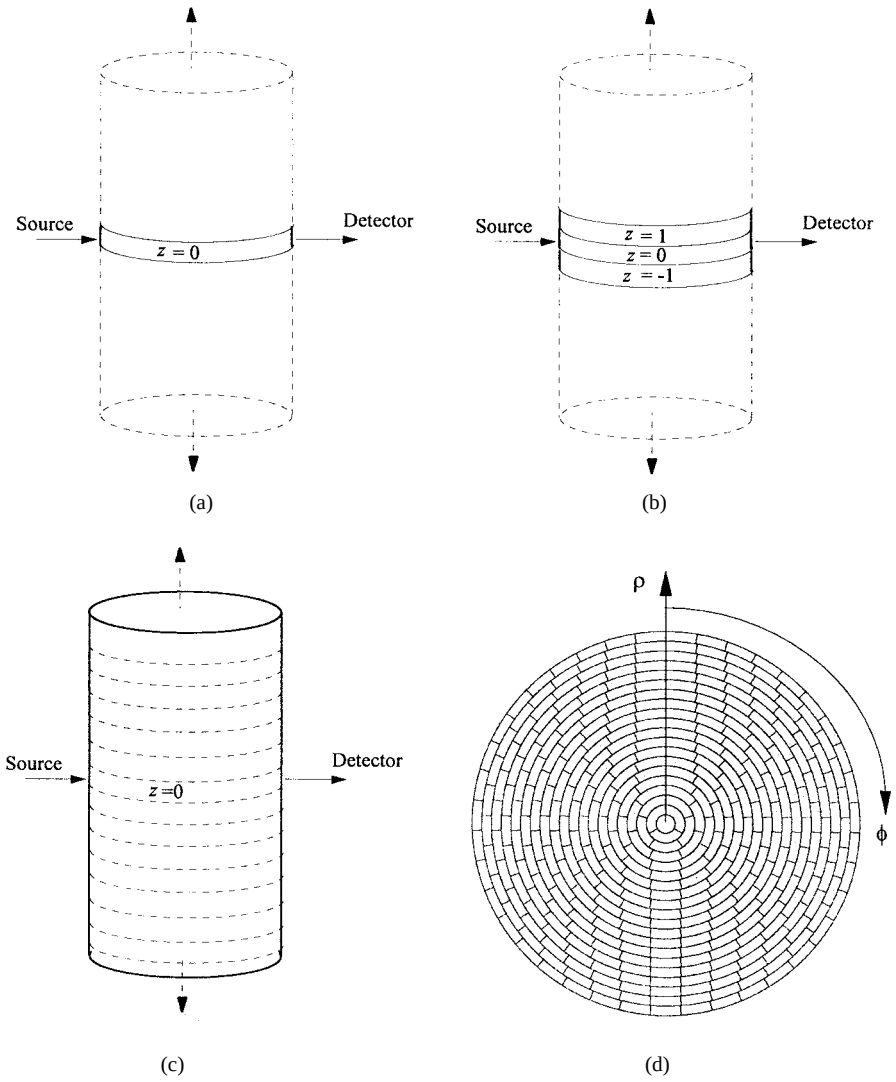

Fig. 6. Three reconstruction types: (a) Type-1 reconstruction, where it is assumed that fluorophore is present only in layer $z = 0$, (b) Type-2 reconstruction, where it is assumed that fluorophore is present only in layers $z = -1$, 0, and 1, and (c) Type-3 reconstruction, where a uniform distribution of fluorophore along the z-axis is assumed. The cylindrical coordinate system used to digitize the phantom is shown in (d).

$\sim$50 μM were embedded in a 8 cm (inside diameter) by 50 cm (height) cylindrical vessel filled with 0.2% Intralipid® (% lipid per unit volume). The same cylindrical vessel was used in the second experiment, this time filled with a 0.33% Intralipid suspension. The background medium also contained Rhodamine 6G at a concentration of 0.1 μM. The volume of the balloon was 0.5 mL, and it was filled with dye at a concentration of 10 μM. In both experiments, a Coherent® Innova® 200-10 argon ion laser source operating in multiline mode (average wavelength $\sim$500 nm) at a power level of 0.75 W was used to irradiate the phantom. This excitation level was used only for purposes of stability, not due to lack of signal; in fact, for some measurements it was necessary to attenuate the measured fluorescence to avoid saturation of the detector. A Newport FS-1 RG.610 filter blocked excitation light from entering the detector. The detector was a Hamamatsu C3140 charge-coupled device (CCD) camera directed normal to the surface of the phantom to collect the emission light.

In the first experiment, the detector was initially located so that the angle between the detector axis and source beam was 90°; the phantom was rotated through 30° clockwise, as viewed from above, after each measurement, until a set of twelve independent detector readings was obtained and the phantom returned to its original orientation; the detector was then revolved 10° counterclockwise about the phantom, increasing the angle between the detector axis and source beam to 100°, and a second set of twelve detector readings was obtained; the detector-revolution/phantom-rotation process was repeated an additional four times, until the angle between the source beam and detector axis was 140°, and a total of 72 detector readings was taken. In the second experiment, the measurement scheme used was similar, except the angle between the detector and source was incremented by 30°, through a total span of 180°, for each new set of measurements until a total of eighty four detector readings was taken.

Dark current was measured after each camera movement. The source intensity was recorded for each measurement using a Coherent Labmaster-E laser measurement system with a model LM-3 detector head. At least two measurements were taken and averaged to obtain the detector readings for each

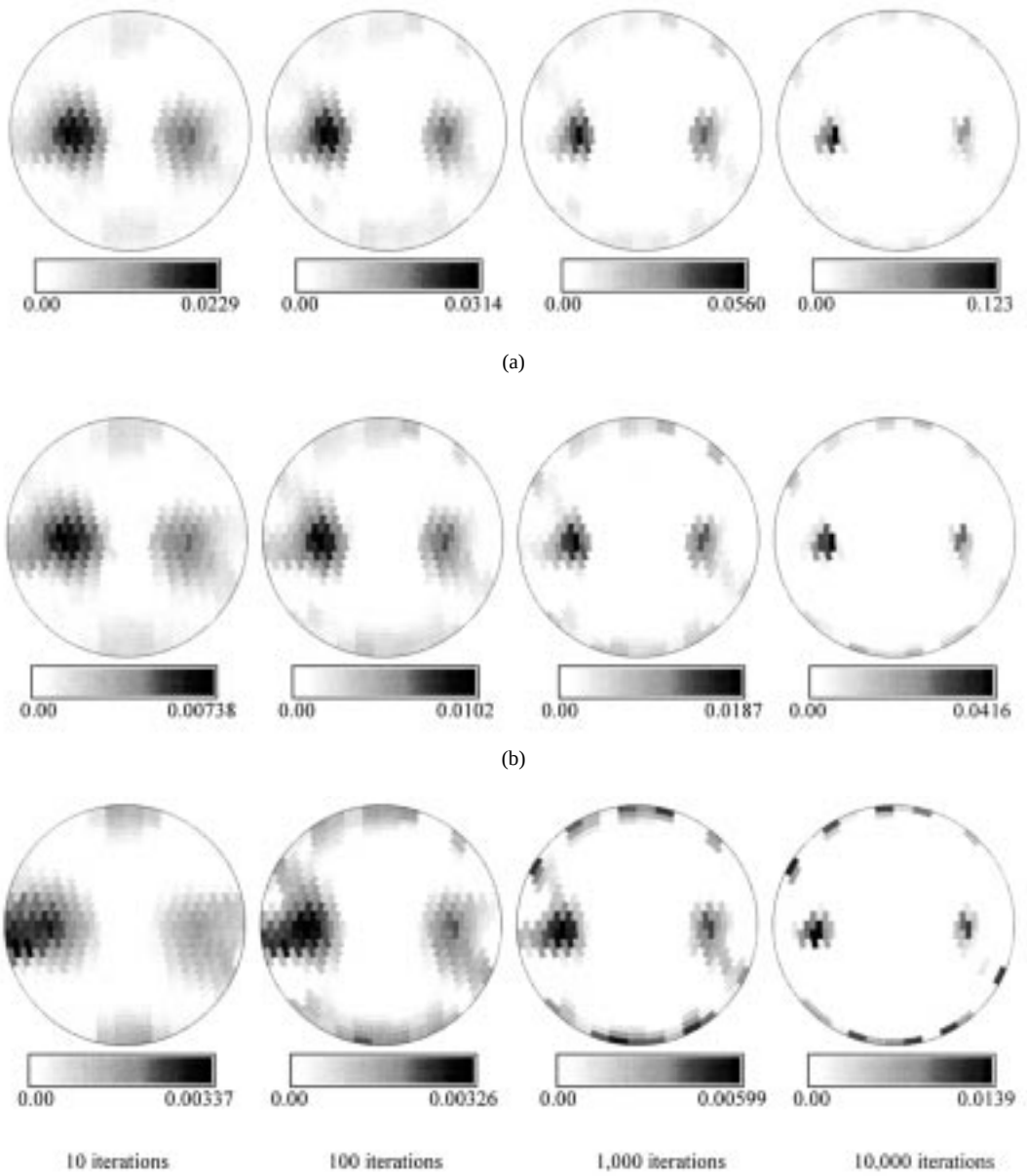

Fig. 7. (a) Type-1, (b) Type-2, and (c) Type-3 images of $\gamma\mu_{T,\,1-2}$ reconstructed from data from the first experiment, using CGD algorithm, after 10, 100, 1000, and 10 000 iterations. Absolute values of the reconstructed quantity, in units of mm^{-1}, are given on the gray scale accompanying each image. The targeted reconstruction value is 0.04 mm^{-1}.

source-detector pair. The CCD camera's detector readings were converted to an estimate of the number of photons exiting the cylinder by multiplying them by the product of the CCD's high gain conversion factor, quantum efficiency, and open area ratio. Two gain settings are available to the camera, with each detector reading unit corresponding to 25 photoelectrons at low gain and to five photoelectrons at high gain; the latter setting was used for all measurements in both experiments. The quantum efficiency for 590-nm wavelength light is used as the average quantum efficiency for the detected infrared light. The maximum quantum efficiency of the CCD is $\sim$25%, and is about 75% of maximum at 590 nm [35]. Because of the interline transfer design of the CCD chip, with paired imaging and readout registers where the latter are located between the former in parallel rows, its open area ratio is 25%. The area on the cylinder's surface seen by the camera, as determined by photographing printed grid patterns taped to the cylinder, is 38.10×31.75 mm. As there are 510×492 pixels on a CCD chip [36], the corresponding area on the cylinder seen by a single pixel can be estimated as $\sim 5 \times 10^{-3}$ mm^2. The solid angle subtended at the camera aperture by a point on the cylinder's surface is the ratio of the aperture area to the square of the distance between the cylinder and aperture, and is $\sim 4 \times 10^{-5}$ sr. The measured angular intensity is thus the number of detected photons divided by the area of a single pixel and the solid angle. This intensity is further normalized to the incident photon rate, which is the incident power divided by the product of the average frequency of an incident photon

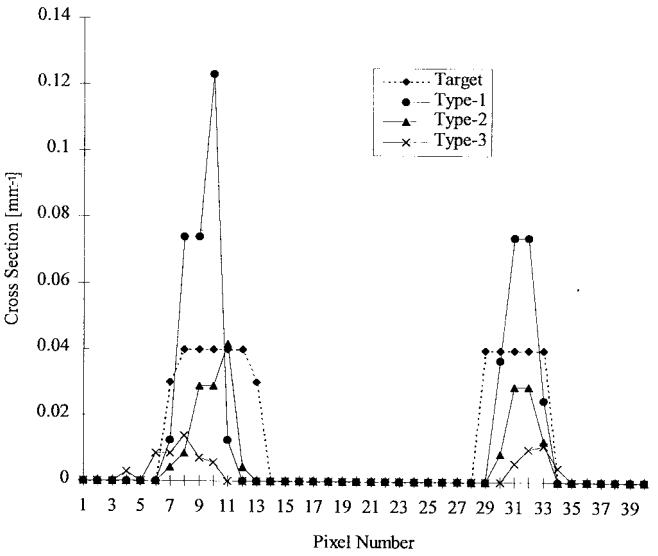

Fig. 8. Plot of reconstructed cross section versus pixel number for the 10 000-iteration images shown in Fig. 8, along the direction bisecting the target's locations. The Type-2 reconstruction gives the best quantitative accuracy, as expected based on the closer agreement between the physical structure of the phantom and the assumption underlying this type than those of the other two types.

and Planck's constant. Under these conditions, the intensity and adjoint used for computation of weight functions are just the Green's functions for a source located at the incident beam and detector locations.

The optical thickness of the phantom medium was estimated as being ~24 and ~40 transport mean free pathlengths (tmfp) for the experiments involving 0.2 and 0.33% Intralipid, respectively [37]. Weight functions for the corresponding reference media were calculated from intensities computed by Monte Carlo simulations of isotropically scattering cylindrical media with optical thicknesses of 24 and 40 mean free pathlengths (mfp).

C. Image Reconstruction

Image reconstructions were performed using three iterative algorithms—POCS [31], CGD [32], and SART [2]. Three types of 2-D reconstructions were performed, as shown in Fig. 6. In the Type-1 reconstruction shown in Fig. 6(a), it was assumed that only voxels bisected by the $z = 0$ plane contain fluorescent dye, and only voxels in this layer were considered in the reconstruction. For the Type-2 reconstruction shown in Fig. 6(b), it was assumed that only voxels bisected by the planes $z = -1$, 0, or 1 contain fluorescent dye and that its concentration along the z-axis is constant within these three layers. In this case, the weights for voxels with the same z-coordinate were summed in these three layers to yield an integrated value. For the Type-3 reconstruction shown in Fig. 6(c), it was assumed that the phantom is invariant along the z-axis, and the weights of all voxels with the same z-coordinate were summed to obtain an integrated value. Only the central plane ($z = 0$) of the reconstruction results is displayed. All three types of reconstruction were carried out on the data from both experiments.

Fig. 4(d) illustrates the cylindrical coordinate system, with the ρ- and ϕ- coordinates are shown in the figure and the z-coordinate normal to the plane of the figure, and the pattern of voxels used in the image reconstructions. There are 400 voxels in each layer, each with a total volume of 16π mm^3; the thickness of each layer in the z-direction is 4 mm.

The quantitative value for the reconstructed property, $\gamma N_0 \sigma_{1\to 2}$, can be estimated if the quantum yield γ and molar extinction coefficient ε are known. The ε for Rhodamine 6G is about 3.2×10^4 cm^{-1}M^{-1} at 500 nm, and its quantum efficiency under CW Ar^+ laser illumination is about 25% [38]. Thus, the target cross sections of the reconstructed results are $\gamma N_0 \sigma_{1\to 2} = 0.04$ mm^{-1} and $\gamma N_0 \sigma_{1\to 2} = 0.008$ mm^{-1} for the first and second experiment, respectively.

D. Results

Fig. 7 shows the images reconstructed from data from the first experiment, using the CGD algorithm, for the three reconstruction types after 10, 100, 1000, and 10 000 iterations. The absolute quantitative accuracy of the image reconstructed by each of the three algorithms is shown in Fig. 8, where we plot one-dimensional (1-D) sections along the diameter that bisects the 10 000-iteration images of the two balloons. In Fig. 9 we compare Type-3 reconstruction results of all three algorithms after 100 and 10 000 iterations. Fig. 10 shows the images reconstructed from data from the second experiment, using the CGD algorithm, for the three reconstruction types after 10, 100, 1000, and 10 000 iterations. One-dimensional sections along the diameter that bisects the 10 000-iteration images of the balloon, for each of the reconstruction types, are plotted in Fig. 11.

V. Discussion and Conclusions

A. Saturation, Sensitivity, and Demodulation

In general, the measurability of a modulated fluorescence signal propagating in a turbid medium is a function of the physical properties of the background scattering medium, the excitation conditions, and the properties of the fluorophore itself. The first of these basically acts as a filter, the effect of which can not easily be predicted for an arbitrary medium and more typically must be explicitly evaluated on a case-by-case basis. Here, we have evaluated the latter two factors, with the aim of identifying conditions for optimal detectability. This is straightforward, because analytic solutions to (3) exist when saturation can be ignored. Results from the sensitivity study (Fig. 3) show that for a fixed intrinsic lifetime τ_0, the fluorescence source strength is sensitive to the product of the modulation radial frequency ω and the mean lifetime τ when $\omega\tau \ll 1$ and is insensitive to it when $\omega\tau \gg 1$. In the $\omega\tau \ll 1$ regime, the optimal modulation frequency f and mean lifetime depends on the definition of sensitivity. When $B(\partial A/\partial\tau)$ and $-\partial\varphi/\partial\tau$ are the sensitivities to be maximized, a fluorophore with as small a τ as possible should be chosen, irrespective of f. On the other hand, when $\tau B(\partial A/\partial\tau)$ and $-\tau(\partial\varphi/\partial\tau)$ are the criteria, the optimal τ is inversely proportional to f. When f is chosen according to the above criteria, demodulation is not a concern because the recommended modulation frequency

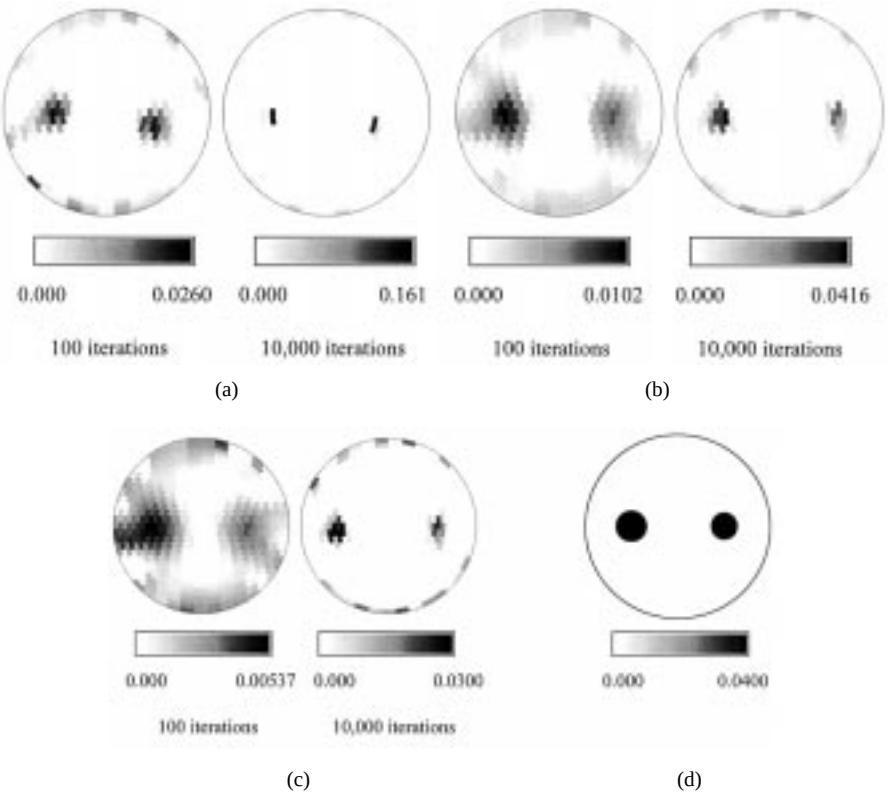

Fig. 9. Type-2 images reconstructed from data from the first experiment, using (a) POCS, (b) CGD, and (c) SART algorithms, after 100 and 10 000 iterations; (d) is the target, where the targeted reconstruction value is $\gamma\mu_{T,1\to 2} = 0.04$ mm^{-1}.

is much smaller than the acceptable upper limit, $f = 1.584/\tau$, that demodulation imposes.

The "$f = 0.159/\tau$ rule" is implicitly supported by the findings of Hutchinson *et al.* [24], who describe a procedure in which a reference probe is used to determine the mean lifetime of a sample probe. In their study, which employed frequency-domain measurements in a highly scattering medium, the phase shifts arising from the fluorescent compounds' mean lifetimes are measured, and the difference between the phase shifts produced by the sample and reference molecules is calculated. Since the phase shift difference is a function of the mean lifetime difference and the mean lifetime of the reference molecule is known, the mean lifetime of the sample molecule can be solved for. Fig. 6 of [24] is a plot of phase-shift difference versus frequency for three sets of molecules with different mean lifetime combinations. Since the phase-shift difference is approximately proportional to phase sensitivity according to our first definition, $-\partial\varphi/\partial\tau$, the modulation frequency producing the maximum phase-shift difference should be close to the optimal frequency we obtain from the $f = 0.159/\tau$ rule. Inspection of the figure reveals that the optimal modulation frequencies are indeed very close to what the rule would have predicted.

As mentioned, here we have studied the properties of a fluorescent compound in isolation, without considering the properties of the background scattering medium in which it may be embedded. It is expected that the presence of a background medium will modify the optimal modulation frequency. One especially important case is when fluorophore distributed throughout the background emits light that competes with the signal from the target. In this case our rules for the optimal sensitivity are subject to modification due to the fact that the total detected signal is a sum of the signals from the background and the target, and typically these would not be in phase. For any mean lifetime, amplitude sensitivity increases monotonically with decreasing modulation frequency. When f is small, mean lifetime fluctuations in the target produce only small changes in the phase of the target signal. Thus, we do not expect significant modification of the result we have derived for optimal amplitude sensitivity. The effect of the background signal on the f for optimal phase sensitivity is a more complex issue, because the phase change in the total signal that is produced by a fluctuation in the target signal depends on the target signal's amplitude as well as on its phase. To ensure that the target signal has sufficient amplitude that it will not be swamped out by the background signal, it may be necessary to use a modulation frequency less than $f = 0.159/\tau$. The exactly optimal modulation frequency will be case-dependent and can not easily be derived analytically.

B. The Inverse Problem

Results in Fig. 7 demonstrate that both balloons are correctly located and the image quality improves with the number of iterations, although artifacts are present, especially at the boundary. The image of the larger balloon has both greater spatial extent and higher image intensity than that of the smaller one. Ideally, both balloons' images would have the same numerical value. This suggests that the inverse prob-

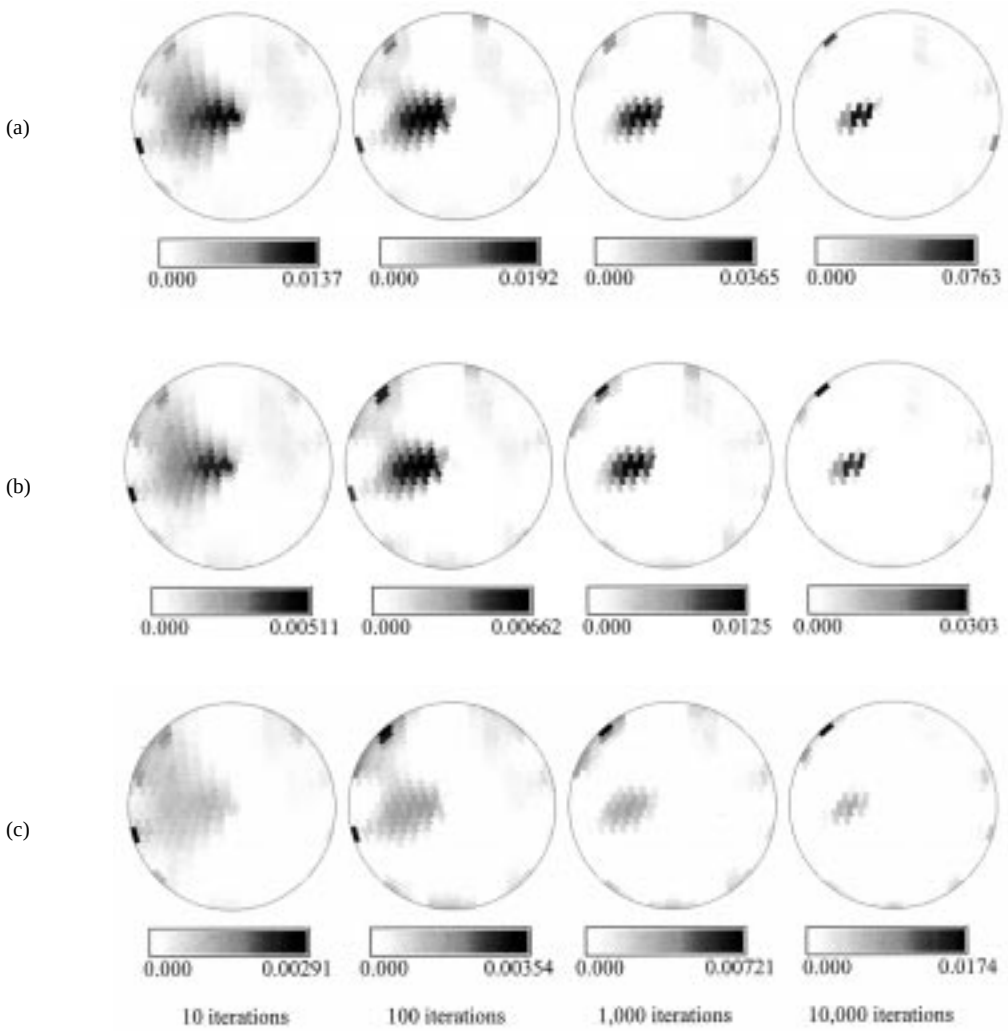

Fig. 10. (a) Type-1 ($z = 0$), (b) Type-2 ($z = -1$–1), and (c) Type-3 ($z = -10$–10). Images reconstructed from data from the second experiment, using the CGD algorithm and all three reconstruction types, after 10, 100, 1000, and 10 000 iterations. The target's absolute value is $\gamma\mu_{T,\,1\to 2} = 0.008$ mm^{-1}.

lem we solved does not have a unique solution and that, within certain limits, size and intensity are interchangeable. This phenomenon is usually a consequence of starting with an underdetermined and/or ill-posed imaging operator. The conditioning of the imaging operator is a function of the number and location of source-detector pairs, and of the size and physical properties of the target medium. As a rule, more source-detector pairs are needed to make the problem more fully determined; however, improperly located source-detector pairs may not lead to any improvement at all. In addition, constraints derived from *a priori* information about the target media, e.g., the positivity constraint adopted in this study, should be used to help confine the reconstruction results.

If we look at only the qualitative results in Fig. 7, we see that the Type-1 and Type-2 reconstructions are about equally good, with the balloons accurately located, while Type-3 is less accurate in terms of the balloon's locations and is more seriously corrupted by artifacts. The absolute value of $\gamma N_0 \sigma_{1\to 2}$ in the reconstructed images usually lies within a factor of 2–3 of the target value, but significant deviations from the target value were observed for some combinations of reconstruction algorithm, reconstruction type, and number of iterations. The quantitative results, as seen in the gray scales of Fig. 7 and in the 1-D profiles of Fig. 8, show that the Type-2 reconstruction provides the most accurate reconstructed values after 10 000 iterations, while Type-1 and Type-3 either overestimate or underestimate the target value. This is not unexpected, since it is Type-2 whose underlying assumptions most closely match the physical structure of the experimental setup.

Results in Fig. 9 show poorly resolved images early in the reconstruction, but distinguishable inhomogeneities are observable for the POCS and CGD algorithms. After 1000 iterations, all three algorithms are able to resolve two inclusions with artifacts. The differences in size and intensity among the three algorithms' results point out different characteristics of each one, in addition to the nonuniqueness problem described above. In an iterative method, the image is updated after each iteration by an amount and in a direction (in the solution space) chosen by the algorithm. Because different algorithms take very different pathways in updating the reconstruction and only a finite number of iterations is allowed, different

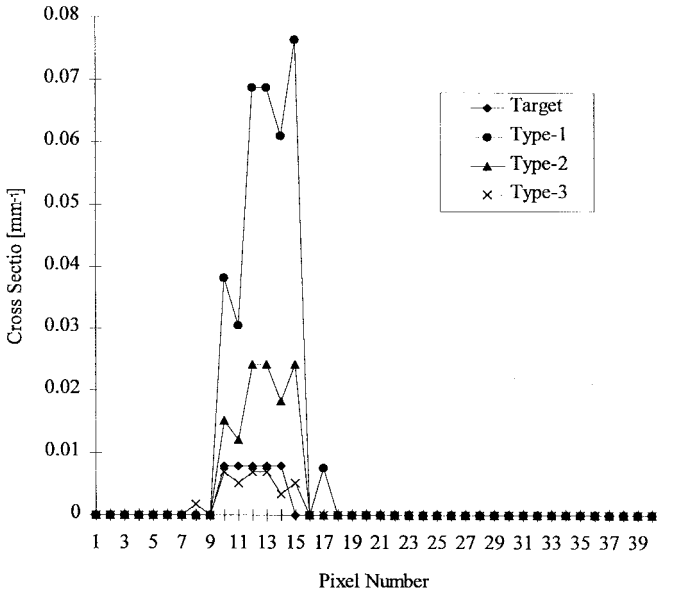

Fig. 11. Plot of reconstructed cross section versus pixel number for the 10 000-iteration images shown in Fig. 10, along the diameter bisecting the target's location. Because of the fluorophore uniformity distributed in the background in this case, the Type-3 reconstruction is expected to have the best quantitative accuracy, and does.

reconstruction results and convergence rates, especially when range constraints are applied, are obtained. Comparing the images reconstructed by the three algorithms, we see that all three accurately locate the balloons, but the spatial extent of their images and the quantitative results are quite different. The POCS algorithm converges much faster than the other two methods, in terms of limiting the spatial extent of the images of the balloons, and produces the least artifact. However, while it produces good results after 100 iterations, the reconstructed size and $\gamma N_0 \sigma_{1\to 2}$ become unreasonable after 10 000 iterations. The SART algorithm, on the other hand, has a low initial convergence rate, but ultimately produces quite accurate target location and quantitative results (0.03 mm^{-1}, while the target value is 0.04 mm^{-1}). The CGD algorithm produce the best reconstruction results of the three in terms of location and quantitative value for $\gamma N_0 \sigma_{1\to 2}$ (0.0416 mm^{-1}).

The results shown in Fig. 10 suggest that all three types of reconstruction successfully located the target while the Type-3 reconstruction was most susceptible to artifacts, as was also observed in the case of the first experiment. In this reconstruction type, the peak quantitative value of the reconstructed $\gamma N_0 \sigma_{1\to 2}$ in the surface artifact was 2–3 times higher than that in the image of the balloon, while in the other two reconstruction types, as is indicated by the gray scales of Fig. 10, the ratio was much closer to unity. This is consistent with the fact that the assumptions underlying the Type-3 reconstruction are most at odds with the physical structure of the phantom, and with the result of a previous study which showed that when there is a systematic mismatch in the weight function, artifacts become more significant [22]. Quantitatively, however, the Type-3 reconstruction produced the most accurate result ($\sim$0.007 mm^{-1} versus 0.008 mm^{-1} target value within the image of the balloon), as shown in Fig. 11. This may be a consequence of the contribution to the total detected signal of the fluorophore uniformly distributed throughout the background scattering medium. Although the concentration of the background fluorophore is only 1% of that in the balloon, the total amount of background fluorophore is many times greater than that in the balloon. This can be demonstrated by calculating the volume of the 12-mm-high disk (i.e., three layers of voxels) of scattering medium in which the balloon lay, which is $\pi(4\text{ cm})^2(1.2\text{ cm}) \approx 60\text{ cm}^3$, more than 100 times greater than that of the balloon. With the range constraints used in the reconstructions, many of the voxels containing background fluorophore end up with their computed value of $\gamma N_0 \sigma_{1\to 2}$ set to zero. Thus the contribution of background fluorescence to the detector readings, which "has to go somewhere" in the reconstructed image, has the effect of increasing the quantitative value of $\gamma N_0 \sigma_{1\to 2}$ for the balloon.

The phenomenon just described could seriously hinder efforts at quantitative fluorescence imaging, because in a real biological environment the background fluorophore concentration could easily be as high as 10% of that in the region of interest. One possible way to overcome this may be to set the lower limit of the range constraints to a reasonable positive constant value, rather than to zero. Another method that may be effective for medium geometries in which detectors can be symmetrically disposed about the source was suggested by O'Leary *et al.* [39]. In this method, pairs of measurements with equal source-detector separations are compared in order to eliminate the homogeneous background contribution.

Our inversion formula allows us to reconstruct only the product of quantum yield and fluorophore concentration when only dc measurements are made. These two factors are not separable because the detector response is proportional to their product and is independent of f [see (7)]. The contribution of mean lifetime to the detector response is, on the other hand, a function of f. Thus, additional measurements at one or preferably several other modulation frequencies are needed to reconstruct τ once γN_0 is found from dc measurements. Then if τ_0 is known, e.g., if it is the same in tissue as *in vitro*, γ and N_0 can be readily computed separately once τ has been solved for.

REFERENCES

[1] J. R. Lakowicz, *Principles of Fluorescence Spectroscopy.* New York: Plenum, 1983.
[2] R. L. Barbour, "Optical tomography and magnetic resonance," presented at *Int. Conf. Future Directions of Lasers in Surgery and Medicine,* Snowbird, UT, July 1995.
[3] D. B. Shealy, M. Lipowska, J. Lipowski, N. Narayanan, S. Sutter, L. Strekowski, and G. Patonay, "Synthesis, chromatographic separation, and characterization of near-infrared-labeled DNA oligomers for use in DNA sequencing," *Analytical Chem.,* vol. 67, pp. 247–251, 1995.
[4] A. V. Kak and M. Slaney, *Principles of Computerized Tomographic Imaging.* Piscataway, NJY: IEEE Press, 1988.
[5] H. Stark, Ed., *Image Recovery: Theory and Application.* New York, NY: Academic, 1987.
[6] A. Ishimaru, *Wave Propagation and Scattering in Random Media.* New York, NY: Academic, 1978.
[7] K. M. Case and P. F. Zweifel, *Linear Transport Theory.* Reading, MA: Addison-Wesley, 1967.
[8] J. Lamarsh, *Introduction to Nuclear Reactor Theory.* Reading, MA: Addison-Wesley, 1966.
[9] M. S. Patterson, B. Chance, and B. C. Wilson, "Time-resolved reflectance and transmittance for the noninvasive measurement of tissue

optical properties," *Applied Optics*, vol. 28, pp. 2331–2336, 1989.
[10] J. Wu, F. Partovi, M. S. Feld, and R. P. Rava, "Diffuse reflectance from turbid media: An analytic model of photon migration," *Appl. Optics*, vol. 32, pp. 1115–1121, 1993.
[11] D. A. Boas, M. A. O'Leary, B. Chance, and A. G. Yodh, "Scattering of diffuse photon density waves by spherical inhomogeneities within turbid media: Analytic solution and applications," in *Proc. National Academy of Science*, vol. 91, pp. 4887–4891, 1994.
[12] J. Wu, M. S. Feld, and R. P. Rava, "Analytic model for extracting intrinsic fluorescence in turbid media," *Appl. Optics*, vol. 32, pp. 3585–3595, 1993.
[13] M. S. Patterson and B. W. Pogue, "Mathematical model for time-resolved and frequency-domain fluorescence spectroscopy in biological tissues," *Appl. Optics*, vol. 33, pp. 1963–1974, 1994.
[14] E. W. Larsen, "Theoretical analysis pencil beams with highly forward scattering," in *OSA Trends in Optics and Photonics on Advances in Optical Imaging and Photon Migration*, R. R. Alfano and J. G. Fujimoto, Eds. Washington, DC: Optical Society of America, 1966, vol. 2, pp. 258–262.
[15] J. Chang, R. Aronson, H. L. Graber, and R. L. Barbour "Imaging diffusive media using time-independent and time-harmonic sources: Dependence of image quality on imaging algorithms, target volume, weight matrix, and view angles," in *Proc. Optical Tomography, Photon Migration, and Spectroscopy of Tissue and Model Media: Theory, Human Studies, and Instrumentation*, Feb. 1995, vol. SPIE-2389, pp. 448–464.
[16] H. L. Graber, J. Chang, R. Aronson, and R. L. Barbour, "A perturbation model for imaging in dense scattering media: Derivation and evaluation imaging operators," in *Medical Optical Tomography: Functional Imaging and Monitoring*, SPIE Institutes vol. IS11., vol. G. Müller *et al.*, Eds. Bellingham, WA: SPIE, 1993, pp. 121–143.
[17] J. Chang, H. L. Graber, and R. L. Barbour, "Luminescence optical tomography," *J. Opt. Soc. Amer. A*, Jan. 1997, to be published.
[18] Y. Yao, R. L. Barbour, Y. Wang, H. L. Graber, and J. Chang, "Sensitivity studies for imaging a spherical object embedded in a spherically symmetric, two-layer turbid medium with photon density waves," *Appl. Optics*, vol. 35, pp. 735–751, 1996.
[19] R. L. Barbour, H. L. Graber, J. Chang, S. S. Barbour, P. C. Koo, and R. Aronson, "MR–Guided optical tomography," *IEEE Computational Sci. & Eng. Mag.*, Winter 1995, vol. 2, pp. 63–77.
[20] J. Chang, H. L. Graber, P. C. Koo, R. Aronson, S. S. Barbour, and R. L. Barbour, "Optical imaging of anatomical maps derived from magnetic resonance images using time-independent optical sources," *IEEE Trans. Med. Imag.*, submitted for publication.
[21] J. Chang, R. L. Barbour, H. Graber, and R. Aronson, "Fluorescence optical tomography," in *Proc. Experimental and Numerical Methods for Solving Ill-Posed Inverse Problems: Medical and Nonmedical Applications*, July 1995, vol. SPIE-2570, pp. 59–72.
[22] J. Chang, H. Graber, R. Aronson, and R. L. Barbour, "Fluorescence imaging using transport-theory-based image operators," in *Proc. 1995 IEEE Engineering in Medicine and Biology 17th Annu. Conf.*, Sept. 1995, pp. 1524–1528.
[23] G. van den Engh and C. Farmer, "Photo-bleaching and photon saturation in flow cytometry," *Cytometry*, vol. 13, pp. 669–677, 1992.
[24] C. L. Hutchinson, J. R. Lakowicz, and E. M. Sevick-Muraca, "Fluorescence lifetime-based sensing in tissues: A computational study," *Biophysical J.*, vol. 68, pp. 1574–1582, 1995.
[25] X. D. Li, M. A. O'Leary, D. A. Boas, B. Chance, and A. G. Yodh, "Fluorescent diffuse photon density waves in homogeneous and heterogeneous turbid media: Analytic solutions and applications," *Appl. Optics*, vol. 35, pp. 3746–3758, 1996.
[26] G. Müller *et al.*, Eds., *Medical Optical Tomography: Functional Imaging and Monitoring*, SPIE Institutes vol. IS11. Bellingham, WA: SPIE, 1993.
[27] *OSA Proceedings on Advances in Optical Imaging and Photon Migration*, R. R. Alfano, Ed. Washington, DC: Optical Soc. Amer., 1994, vol. 21.
[28] E. Fukushima and S. B. W. Roeder, *Experimental Pulse NMR: A Nuts and Bolts Approach.* Reading, MA: Addison-Wesley, 1981, pp. 6–7.
[29] M. A. O'Leary, D. A. Boas, X. D. Li, B. Chance, and A. G. Yodh, "Fluorescence lifetime imaging in turbid media," *Optics Lett.*, vol. 21, pp. 158–160, 1996.
[30] D. Y. Paithankar and E. M. Sevick-Muraca, "Fluorescence lifetime imaging with frequency-domain photon migration measurement," in *OSA Trends in Optics and Photonics on Biomedical Optical Spectroscopy and Diagnostics*, vol. 3, E. Sevick-Muraca and D. Benaron, Eds. Washington, DC: Optical Soc. Amer., 1996, pp. 184–194.
[31] D. C. Youla, "Mathematical theory of image restoration by the method of convex projections," in [5].
[32] P. E. Gill, W. Murray, and M. H. Wright, *Practical Optimization.* New York, NY: Academic, 1981.
[33] NCRP Scientific Committee 52, "Conceptual basis for calculations of absorbed-dose distribution," NCRP Tech. Rep. 108, 1991.
[34] H. C. van de Hulst, *Multiple Light Scattering: Tables, Formulas, and Applications.* New York, NY: Academic, 1980, vol. 1, ch. 3.
[35] Hamamatsu Photonics Systems, Bridgewater, NJ, personal communication.
[36] Hamamatsu Photonics Systems, *Cooled CCD C3140 (for C2280-60) Instruction Manual.*
[37] H. J. van Staveren, C. J. M. Moes, J. van Marle, S. A. Prahl, and M. J. C. van Gemert, "Light scattering in Intralipid—10% in the wavelength range of 400–1100 nm," *Appl. Optics*, vol. 30, pp. 4507–4514, 1991.
[38] U. Brackmann, *Lambdachrome Laser Dyes.* Lambda Physik GmbH: Göttingen, Germany, 1986, pp. III-116–III-117.
[39] M. A. O'Leary, D. A. Boas, B. Chance, and A. G. Yodh, "Experimental images of heterogeneous turbid media by frequency-domain diffusing-photon tomography," *Optics Lett.*, vol. 20, pp. 426–428, 1995.

Jenghwa Chang (S'92–M'95) was born in 1962 in Taipei, Taiwan, R.O.C. He earned the B.S. and M.S. degrees from the Department of Control Engineering and the Institute of Communication Engineering, National Chiao-Tung University, Hsin-Tsu, Taiwan, ROC, in 1984 and 1986, respectively. He received the Ph.D. degree in electrical engineering from Polytechnic University of New York, Brooklyn, NY, in 1994.

Currently, he is a Research Assistant Professor in the Department of Pathology of the SUNY Health Science Center at Brooklyn, NY, and is a Medical Physicist specializing in radiation oncology. His research interests include medical imaging, signal processing, electromagnetics, medical physics, and biomedical informatics.

Dr. Chang is a member of AAPM and AAAS. His WWW page is available at: http://challenge.path.hscbklyn.edu/chang.

Harry L. Graber (S'94–A'96) was born in 1961 in New York. He earned the A.B. degree with a concentration in chemistry from Washington University, St. Louis, MO, in 1983 and will receive the Ph.D. degree from the Program in Physiology and Biophysics of the SUNY Health Science Center at Brooklyn, NY, in 1997.

His research interests in biomedical optics, medical imaging, and medical physics.

Mr. Graber is a member of the Biophysical Society and the Optical Society of America.

Randall L. Barbour (M'95) earned the Ph.D. degree in biochemistry from Syracuse University, Syracuse, NY, in 1981.

He is a Professor of Pathology and Biophysics and Director of Clinical Chemistry at the State University of New York Health Science Center at Brooklyn, NY. He is also a Research Professor of Electrical Engineering at Polytechnic University of New York, Brooklyn. He has written numerous papers on methods for imaging in random media and on the application of noninvasive methods for the study of organ function.

Dr. Barbour is a member of the American Association for Clinical Chemistry and FASEB. He is active in SPIE and has recently chaired conferences on medical imaging and numerical methods for solving ill-posed inverse problems. He also serves on National Institutes of Health (NIH) study sections for diagnostic imaging, lasers, and spectroscopy.